ACS NANO
Cite This: ACS Nano 2018, 12, 3898–3907
www.acsnano.org

ARTICLE

# A Biomimetic Conductive Tendril for Ultrastretchable and Integratable Electronics, Muscles, and Sensors

Yin Cheng,[†,⊥] Ranran Wang,[‡,⊥] Kwok Hoe Chan,[†] Xin Lu,[†] Jing Sun,[‡] and Ghim Wei Ho*[,†]

[†]Department of Electrical and Computer Engineering, National University of Singapore, 4 Engineering Drive 3, Singapore 117583, Singapore

[‡]State Key Laboratory of High Performance Ceramics and Superfine Microstructure, Shanghai Institute of Ceramics, Chinese Academy of Sciences, Shanghai 200050, China

Supporting Information

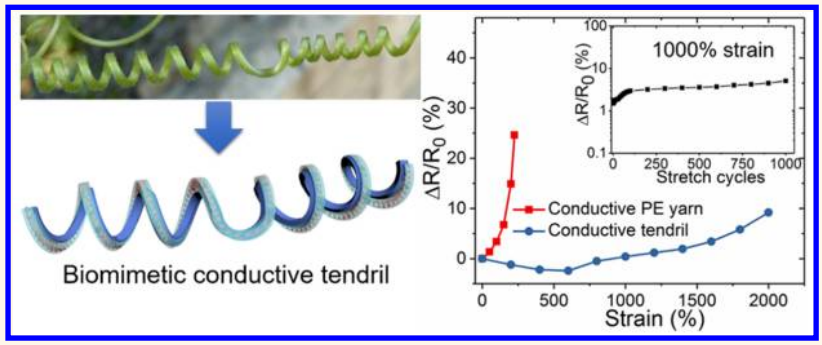


**ABSTRACT:** **Adaptive tendril coiling of climbing plants has long inspired the artificial soft microsystem for actuation and morphing. The current bionic research efforts on tendril coiling focus on either the preparation of materials with the coiling geometry or the design of self-shaping materials. However, the realization of two key functional features of the tendril, the spring-like buffering connection and the axial contraction, remains elusive. Herein, we devise a conductive tendril by fusing conductive yarns into tendril configuration, bypassing the prevailing conductivity constraints and mechanical limitations. The conductive tendril not only inherits an electrophysiology buffering mechanics with exceptional conductance retention ability against extreme stretching but also exhibits excellent contractive actuation performance. The integrative design of the ultraelastic conductive tendril shows a combination of compliant mobility, actuation, and sensory capabilities. Such smart biomimetic material holds great prospects in the fields of ultrastretchable electronics, artificial muscles, and wearable bioelectronic therapeutics.**

**KEYWORDS:** *biomimetic tendrils, compliant mobility, ultrastretchable electronics, artificial muscles, wearable strain sensors*

Plants in nature have evolved with intriguing and vital motility in diversified forms, such as bending of wheat awns,[1] snapping of Venus flytrap,[2] opening of seedpods,[3] and coiling of climbing plant tendrils.[4] Among these plants, the tendril shows fascinating hybrid motion modes, that is, bending and chiral twisting including manifestations of helical curling and morphing, which prove to be highly responsive to variable ambient conditions. Previous studies based on tendril anatomy and cytochemistry revealed the key mechanism of the coiling lies in the differential contraction induced by internal strain mismatch within the tendril tissues, leading to its intrinsic curvature.[4−6] Currently, intense bionic research efforts on the tendril coiling mainly focus on two areas. One is introducing specific built-in strain mismatch into synthetic materials to obtain the same coiling geometry for improved properties. For instance, helical assembly of aligned multiwalled carbon nanotube (MWCNT) fibers with helical gaps for solvent-triggered rotation[7] and helical porous microfibers from polystyrene and polyvinylidene fluoride for improved oil sorption[8] has been realized. The other scope is to design self-shaping materials featuring tunable internal stress in response to specific external stimuli, such as humidity,[9,10] temperature,[11,12] and light irradiation.[13−17]

Despite these achievements, researchers have long overlooked two significant functional competencies of the tendril plant from the biomechanical perspective. For one thing, the coiling structure of the tendril provides the plant with an elastic

Received: February 20, 2018
Accepted: March 27, 2018
Published: March 27, 2018





DOI: 10.1021/acsnano.8b01372
ACS Nano 2018, 12, 3898–3907

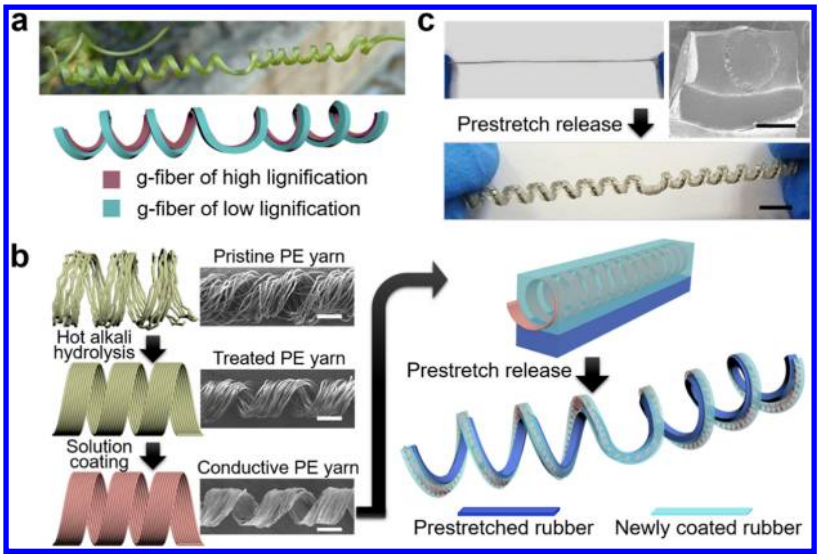


**Figure 1. The design and fabrication of the biomimetic conductive tendril. (a) The coiling model of a cucumber tendril. (b) The schematic illustration of the fabrication process of the conductive tendril. Scale bar for the SEM images, 400 μm. (c) The photographs of the conductive tendril before (upper) and after (lower) prestretch release. Upper-right SEM image shows the cross section of the conductive tendril. Scale bar of the conductive tendril photograph, 4 mm. Scale bar of the SEM image, 400 μm.**

spring-like buffering connection to the nearby anchored support for enhanced tolerance against strong wind and other external impacts.[18,19] For another, the tendril coiling process shortens its length axially and hoists the plant to the grasped point for more advantageous ecological niches (rich sunshine and space, *etc.*), serving as a contracting actuator.[20,21] Both the buffering connection and the contraction actuation of the coiled tendrils are critical for the competitive plant growth, yet rarely explored for the development of biomimetic soft materials.

Herein, we devise a conductive tendril by judiciously incorporating helical conductive yarns into an elastic polymer-based coiled structure to conceptualize ultrastretchable and integratable electronics, muscles, and sensors. The conductive tendril readily inherits the functional merits of its counterpart in nature, including the buffering connection for stretchable conductors and the contraction for actuators. Notably, the mechanical properties of the conductive tendril are tunable *via* the modulation of the predefined strain mismatch. On the one hand, the conductive tendril as opposed to the typical conductive yarn can efficiently accommodate stretch impact *via* coil extension with an unrivalled boost of stretchability from 225% to 2000%, accompanied by significantly improved conductance retention ability: from 24.6% resistance increase to 9.2%. On the other hand, with the conductive yarns as dynamic components in collaboration with the tendril structure, the conductive tendril succeeds in converting electrothermal energy into mechanical contraction, exhibiting excellent actuation performance that displays a contraction stroke of 19.8% and lifting of 120 times its own weight. Moreover, the conductive tendrils can be harnessed as artificial muscles, capable of not only working independently as an elastic dragger on ground and under water but also implementing programmable and sophisticated motility in an integrative level for complex tasks, such as a smart gripper for picking up and putting back objects. Finally, encouraged by the mechanical compliance and stable conductivity, we further modified the conductive tendrils into wearable capacitive strain sensors for various bioelectronic therapeutics such as sleep quality monitoring and hand gesture recognition.

## RESULTS AND DISCUSSION

**Design Concept and Fabrication.** Though research interest around the climbing plant tendril lasts for more than a century, it is until recently that findings indicate a widespread gelatinous fiber (g-fiber) in tendrils dominated the coiling process.[5,6] More precisely, Gerbode *et al.* proved that the g-fiber in cucumber tendril consists of two cell layers, with the layer closer to the concave of the tendril being more heavily lignified than the other layer. Preferential contraction of the highly lignified layer compared with the low lignified layer generates strain mismatch at the interface of the g-fiber, resulting in the intrinsic curvature and coiling of the tendril.[4] The topological conservation law explains the existence of a chiral perversion in the middle of oppositely handed helices with equal coil numbers, given the fixed boundary conditions,[22] as seen in Figure 1a of a cucumber tendril. The fabrication process of the conductive tendril is shown in Figure 1b (detailed fabrication process in Figure S1 and Experimental Methods). The key concept for the design lies in the incorporation of a helical conductive yarn into an elastic polymer layer, which is coated on another prestretched one. After the release of prestretch, the strain mismatch at the interface gives the conductive tendril an intrinsic curvature and it self-shapes into the coiled structure featuring perversion in between oppositely handed helices with equal numbers, as shown in Figure 1c and Movie S1. The scanning electron microscope (SEM) figure of the cross section of the conductive tendril in Figure 1c reveals a clear bilayer structure (thickness of ~1 mm, width of ~1 mm) with the helical conductive yarn embedded into the upper layer (thickness of ~0.6 mm). The helical polyester (PE) yarn, composed of a bunch of PE fibers, is rationally chosen as the precursor yarn for the preparation of conductive PE yarns. The pristine PE yarn is first treated by means of hot alkali hydrolysis, which involves both heat-setting and surface topochemical modification.[23] This treatment not only endows the treated PE yarn with a more compact and consolidated helical structure (SEM figures in Figure 1b) but also changes the PE yarn surface from hydrophobic to hydrophilic (Figure S2 for detailed characterization). The



DOI: 10.1021/acsnano.8b01372
ACS Nano 2018, 12, 3898−3907

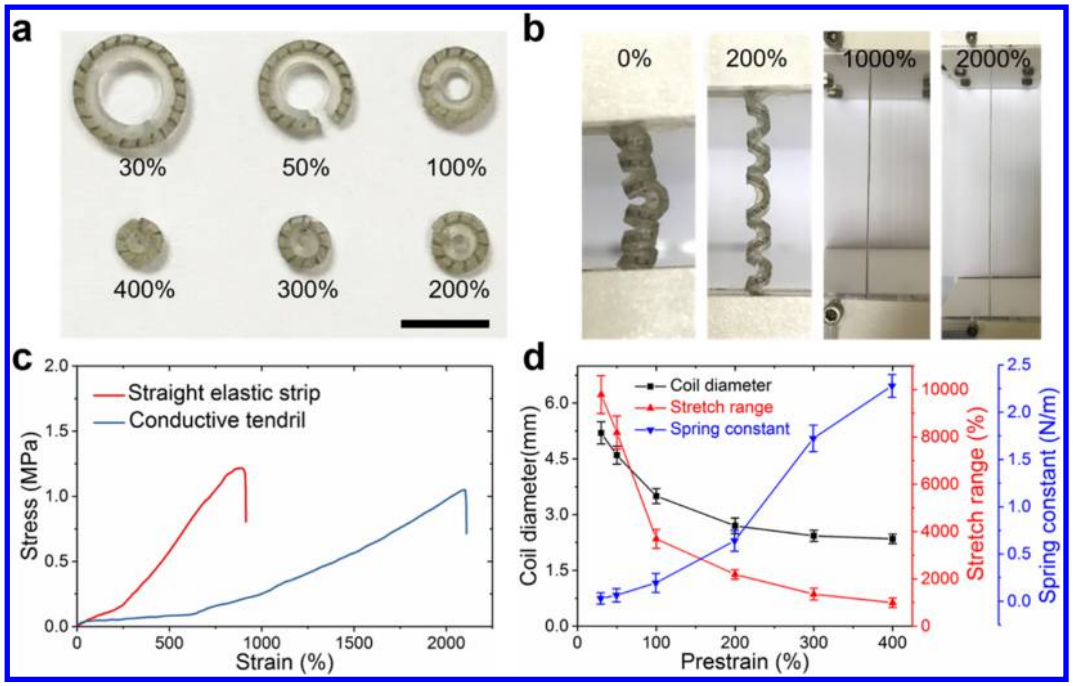


**Figure 2. Mechanical properties of the conductive tendril. (a) The photographs of the conductive tendrils with various prestrains. Scale bar, 4 mm. (b) Photographs of the conductive tendrils with prestrain of 200% being stretched to strain of 2000%. (c) The stress−strain curves of the straight elastic strip and the tendril-structured elastic strip with prestrain of 200%. (d) The coil diameter, stretch range, and spring constant of the conductive tendrils with varying prestrains from 30 to 400%.**

hydrophilicity of the treated PE yarn is indispensable for the subsequent solution coating of conductive inks, for example, the silver nanowire (AgNW) coating as seen in Figure 1b.

**Tuning of Mechanical Properties.** To tune the mechanical properties, we first studied the mechanism of the coiling through adopting the similar mechanical model used for a heated bimetallic strip by Timoshenko and derived the expression of the tendril curvature (see detailed modeling and fitting in Supporting Information and Figures S3 and S4):[24]

$$k = \frac{6\varepsilon(1+m)^2}{(t_1+t_2)\left[3(1+m)^2 + (1+mn)\left(m^2 + \frac{1}{mn}\right)\right]} \quad (1)$$

where $\varepsilon$ is the prestrain (strain mismatch of the two layers for fabrication), $m = t_1/t_2$ ($t_1$ and $t_2$ are the thickness of the prestretched and newly coated layers, respectively) ,and $n = E_1/E_2$ ($E_1$ and $E_2$ are the Young's moduli of the prestretched and newly coated layers respectively). Obviously, $t_1$, $t_2$, $m$, and $n$ are constants because of the specific materials (silicone rubber of Ecoflex 00-30) and controlled layer thickness for fabrication. Consequently, the prestrain determines the curvature of the tendril predominantly in a proportional relationship. Guided by this, we fabricated a series of conductive tendrils with varying prestrains from 30 to 400% as seen in Figure 2a. The radius of curvature of these conductive tendrils decreases with the increase of prestrains, which conforms to the predication in eq 1.

We further investigated the mechanical properties of the conductive tendrils by mechanical tensile tests. Take the conductive tendril with prestrain of 200% as an example: The conductive tendril behaved exceedingly "softer" to stretch as the coiled structure could efficiently accommodate imposed stretch by unwinding and lengthening to its maximum (the stretch process in Figure 2b). Compared with the straight elastic strip, the conductive tendril exhibited a largely extended elastic stretch range, from strain of 910% to 2100%, as shown in the stress−strain curves in Figure 2c. A strain distribution comparison of the straight and coiled structures is shown in Figure S5 to further verify this buffering effect. The coil diameter, stretch range, and spring constant (see measuring method in Supporting Information) of conductive tendrils with different prestrains were measured and plotted in Figure 2d. As the prestrain increased from 30 to 400%, the coil diameter decreased from 5.2 to 2.3 mm and stretch range decreased from 9800 to 990%. In contrast, the spring constant rose up from 0.03 to 2.27 N/m. The testing results imply the increased prestrain gives rise to thinner conductive tendrils with higher spring stiffness. Thus, we can obtain conductive tendrils with desired geometric parameters and mechanical properties with ease by adjusting the prestrain value for different application scenarios.

**Elastic Buffering of the Conductive Tendrils for Ultrastretchable Electronics.** The conductive PE yarn, which imparts conductivity to the tendril, is derived from the treated PE yarn through solution coating strategy. The treated PE yarn is chosen as the helical scaffold for conductive percolation networks for three reasons: (1) the porous structure generated large surface area for construction of conductive networks; (2) the hydrophilicity enabled the effective coating of water/ethanol-based dispersion of different conductive materials; and (3) the helical configuration provided stretchability for the conductive PE yarn. To show the versatility of the treated PE yarn as scaffold for solution coating strategy, we accomplished the building of conductive percolation networks using four different kinds of conductive materials (detailed coating process in Experimental Methods): reduced graphene oxide (RGO) through dip-coating and chemical reduction, MWCNT through dip-coating, Ag particle through solution-based electroless chemical deposition, and


DOI: 10.1021/acsnano.8b01372
ACS Nano 2018, 12, 3898−3907

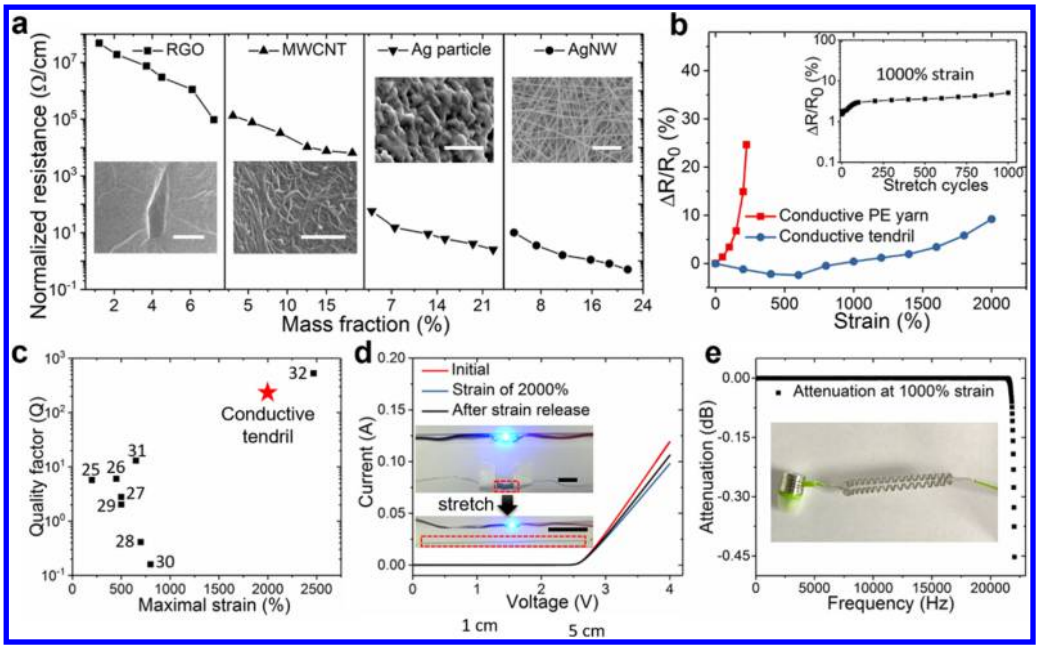


**Figure 3. The properties of the conductive tendril as stretchable conductor. (a) Dependence of the conductance (characterized with normalized resistance to the length of the conductive PE yarns) of conductive PE yarns on the mass fraction of different conductive materials including RGO, MWCNT, Ag particle, and AgNW. Insets are the SEM images of the conductive percolation networks of individual conductive materials coated on the PE fiber surface. Scale bars for the SEM images are 1, 0.5, 2, and 2 μm, respectively. (b) The relative resistance variation of the conductive PE yarn and the conductive tendril *versus* the applied stretch strain. Inset is the relative resistance variation under cyclic stretching test at strain of 1000% up to 1000 cycles. (c) The *Q* values comparison of the conductive tendril with those of stretchable conductors in previous representative papers. (d) The current−voltage curves of a LED at initial, stretching (strain of 2000%), and releasing states. Insets are the photographs of the LED before and after stretching of the conductive tendril. Scale bars for the upper and lower photographs are 1 and 5 cm, respectively. (e) Audio attenuation test with the conductive tendril as the audio cable under stretching. A swept sine wave in the audible frequency range was applied to assess the attenuation under stretch strain of 1000% compared with the audio output under no stretch. Inset shows the photograph of the conductive tendril as the audio cable for the earphone.**

AgNW through dip-coating and annealing. These building blocks coated uniformly on the surface of the treated PE yarn, as seen in SEM images in Figure 3a and Figure S6. Furthermore, the mass fraction of the conductive materials can be readily adjusted *via* the dip-coating or chemical deposition cycles (Figure S7). Due to the different intrinsic conductivities, the corresponding individual conductive PE yarns exhibited different conductance ranges (characterized using normalized resistance to the length of the conductive PE yarns) which enables a widely tunable range from ∼0.5 Ω/cm to 47.6 MΩ/cm as seen in Figure 3a.

The elastic buffering effect of the tendril structure appropriately manifests itself in the utilization of the conductive tendril for ultrastretchable electronics. Here conductive tendril (based on AgNW with normalized resistance of 0.5 Ω/cm to the length of the conductive PE yarn) with prestrain of 200% is used for investigation, considering the desired combination of large stretch range (2100%) and compactness for easy deployment (coil diameter as small as 2.7 mm). Figure 3b displays the relative resistance variation *versus* the stretch strain of both the conductive PE yarn and the corresponding conductive tendril. The conductive PE yarn exhibited a stretch range of 225% owing to its helical structure (optical images of the structure variation during stretch in Figure S8) and a sharp increase of resistance by 24.6% due to micro cracks generation in the conductive network (Figure S9). In comparison, the conductive tendril indicated a markedly expanded stretch range up to 2000% (rupture strain of ∼2100%) and an appreciably slower resistance increase: 1.5% increase at strain of 1000% and 9.2% at 2000%. Further cyclic stretching test (inset of Figure 3b) revealed a reliable durability of the conductive tendril: 5.1% increase of resistance after 1000 times of 1000% strain stretch tests. This significantly improved conductivity retention capability against stretch deformation is attributed to the elastic buffering connection effect of the tendril structure, which greatly mitigates the actual strain on the constituent materials (the conductive percolation network here) by reversible structural adaptation. Besides, the polymer encapsulation might also help inhibit the initiation and propagation of micro cracks, which could contribute to the slow resistance increase. Obviously, the buffering connection effect also applies equally to conductive tendrils based on other conductive materials, including RGO, MWCNT, and Ag particle, as confirmed in Figure S10.

Figure 3c summarizes the quality factor *Q* (defined as the percent strain divided by the percent resistance change) at the maximal stretch strain from previously reported papers for performance comparison. The *Q* value of the conductive tendril (*Q* of 214 at strain of 2000%) are superior to most of the reported works,[25−31] such as crumpled graphene sheets on prestretched substrate (6 at 450%),[26] copper nanowire (CuNW) network transferred onto a helical polydimethylsiloxane (PDMS) substrate (0.41 at 700%),[28] conductive ionic liquids deposited within rubber fiber (0.16 at 800%),[30] and comparable to the state-of-the-art result: a coiled CNT-based core−sheath fiber (526 at 2470%).[32] It is worth noting that the initial resistance of the conductive tendril can be tuned down to 0.5 Ω/cm (as the tested sample in Figure 3b), which is much lower than that for the coiled CNT-based core−sheath fiber (single-ply fiber of ∼600 Ω/cm, seven-ply fiber of ∼100 Ω/



DOI: 10.1021/acsnano.8b01372
ACS Nano 2018, 12, 3898−3907

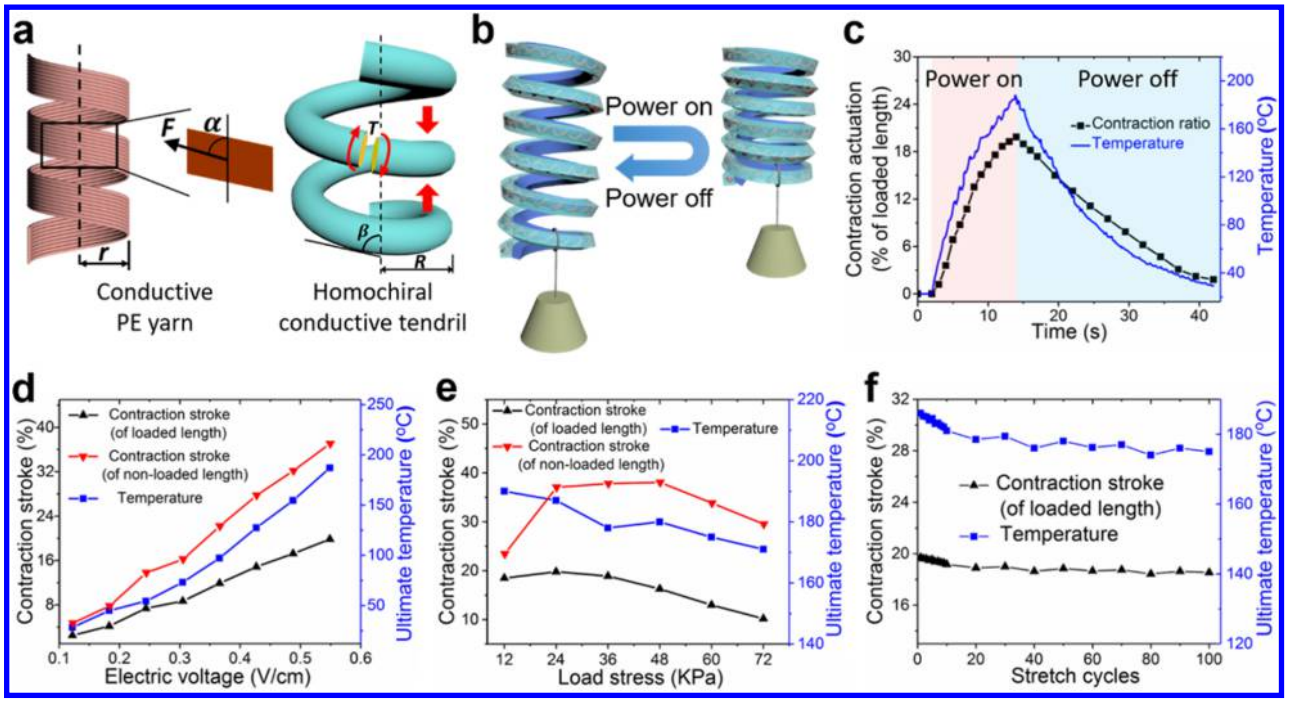


**Figure 4. The mechanism and properties of the conductive tendril as contraction actuators. (a) Schematic diagram of the contraction actuation mechanism. Here assume the upper end of the conductive PE yarn was anchored. (b) The schematic diagram of the conductive tendril working as reversible contraction actuator under electric power with loading. (c) The contraction ratio and temperature change of the conductive tendril during power on (0.55 V/cm for 12 s) and off. (d) The contraction stroke and ultimate temperature of the conductive tendril under load stress of 24 KPa with varying electric voltage from 0.12 to 0.55 V/cm. (e) The contraction stroke and ultimate temperature of the conductive tendril under electric voltage of 0.55 V/cm with varying load stress from 12 to 72 KPa. (f) The contraction stroke and ultimate temperature of the conductive tendril under load stress of 24 KPa and electric voltage of 0.55 V/cm after stretch tests at strain of 1000% up to 100 cycles.**

cm). In addition, the near invariance of conductance during extreme stretching was supplemented by markedly small resistance increase under harsh bending and twisting tests: ~1% of increase at bending radius of 1 mm (Figure S11) and ~8% increase at twisting level of 1000 turns/meter (Figure S12).

The conductive tendril makes an excellent candidate in applications of ultrastretchable electronics by virtue of the notably stable conductance under extreme deformations. Two application demonstrations including ultrastretchable LED lighting and earphone are presented here. Figure 3d displays the current−voltage curves of a LED when the conductive tendril as electric circuiting was stretched to strain of 2000% and then released back. The current decreased by a small extent at ultimate strain and recovered partly after strain release. Also, no conspicuous brightness degradation was noticed during the stretching (the inset in Figure 3d and Movie S2), bending (Movie S3) and twisting tests (Movie S4). Figure 3e examines the audio quality of an earphone with the conductive tendril as the audio cable under stretch test. The result showed there was minimal audio attenuation within the audible frequency range (20−20K Hz) at strain of 1000%, compared with the audio output under no stretch. It was more vividly demonstrated when the conductive tendril served as the audio cable for a speaker to play music (Movie S5).

**Contraction Actuation of the Conductive Tendrils for Artificial Muscles.** The deliberately introduced prestrain during fabrication enabled the autonomous formation of tendril structure. The conductive PE yarns, as a dynamic component, further endowed the conductive tendril with an ability of reversible contraction actuation. The actuation mechanism is schematically illustrated in Figure 4a (see detailed actuation mechanism analysis in Supporting Information and Figures S13−S17). In brief, as the PE fibers possess a negative linear thermal expansion coefficient,[33] Joule heating of the conductive network generates internal contractive force $F$ in the conductive PE yarn along the helix line direction (coil radius of $r$ and helix angle of $\alpha$), which resultantly causes a torque $T$ in the conductive PE yarn. After being incorporated into the homochiral tendril structure (left-handed one, coil radius of $R$ and helix angle of $\beta$), the torque drives the contraction of the conductive tendril. For a conductive tendril with contour length of $l$, the axial contraction distance $d$ can be derived as eq 2:

$$d = R \times \left(1 - \cos\frac{l \sin\beta}{R}\right) \times \sin\left(\frac{lr \sin\alpha}{I_p G} \times F\right) \quad (2)$$

where $I_p$ and $G$ are the polar moment of inertia and the modulus of rigidity of the conductive tendril, respectively. In this expression, for a specific conductive tendril, the parameters are constants except for the heating induced contractive force $F$ in the conductive PE yarn, which is the driving force for the actuation and increases with the elevated temperature.

Conductive tendril with prestrain of 400% was chosen as the actuator, considering that the high spring constant (2.27 N/m) favored the promoted loading capacity. To assess the actuation performance under loading condition, electric power was used to stimulate the conductive tendril (based on AgNW with normalized resistance of 0.5 Ω/cm to the length of the conductive PE yarn) to deliver contraction work, as depicted in Figure 4b. Figure 4c shows the contraction ratio (of loaded



DOI: 10.1021/acsnano.8b01372
ACS Nano 2018, 12, 3898−3907

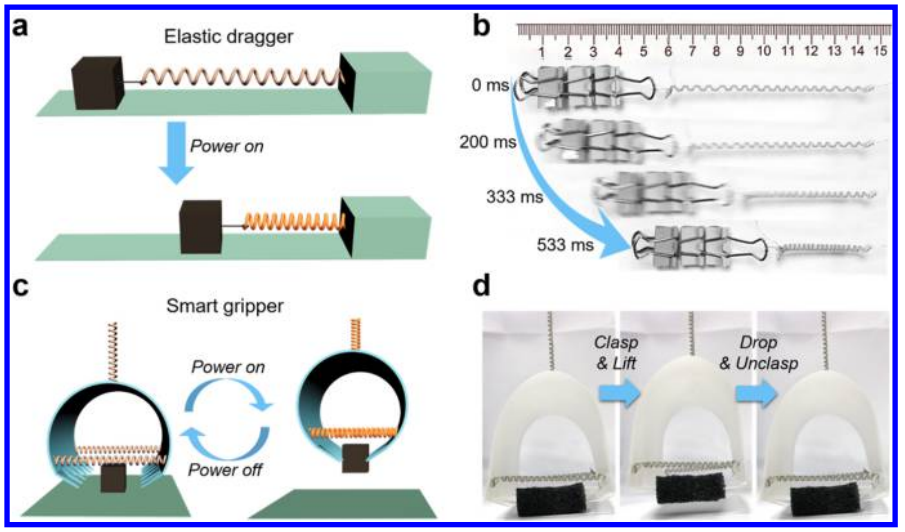


**Figure 5. The conductive tendrils as artificial muscles in applications of a dragger and a smart gripper. (a) The schematic illustration of the conductive tendril working as an elastic dragger on ground. (b) The elastic dragger pulled the load forward by 4.5 cm within 533 ms on ground. (c) The schematic illustration of the integration of conductive tendrils into a smart gripper. (d) The smart gripper picked up and then put down a target object (black polymer foam, 2.8 × 2.8 × 1.2 cm) in a controllable manner.**

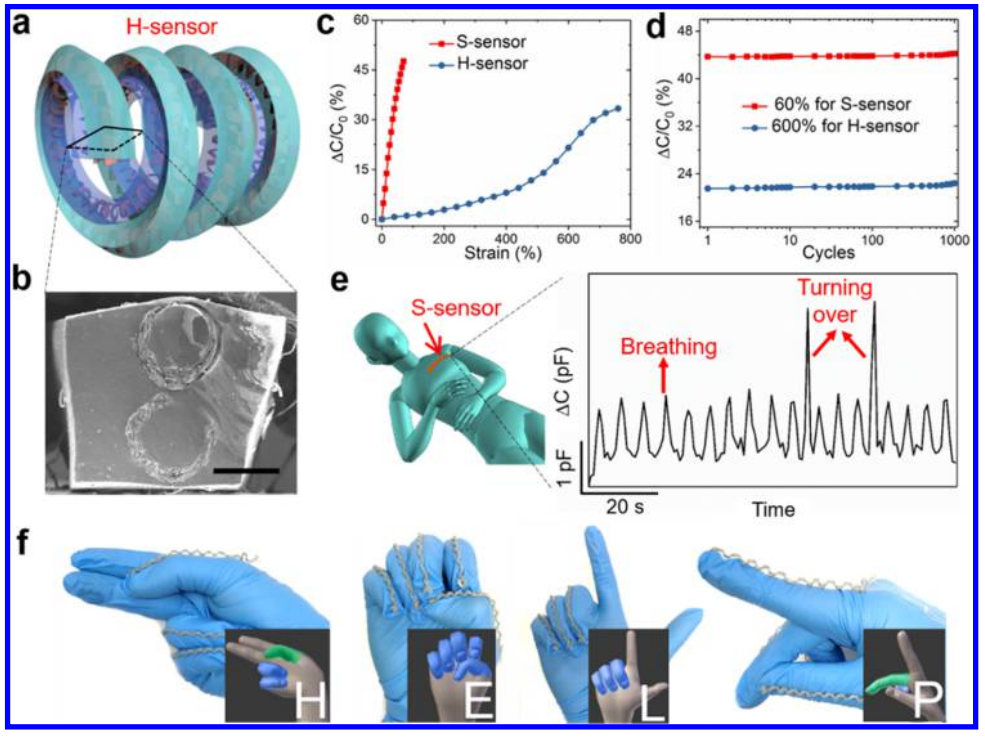


**Figure 6. The conductive tendrils as capacitive strain sensors for wearable sensing applications. (a) The schematic diagram of the H-sensor structure. (b) The SEM image of the cross section of the H-sensor. Scale bar, 500 μm. (c) The relative capacitance change of the S-sensor and the H-sensor *versus* the tensile strain. (d) The durability tests of the S-sensor (testing strain of 60%) and the H-sensor (tensing strain of 600%) for 1000 testing cycles. (e) The application of S-sensor for sleep quality monitoring through recording the breathing and turning over signals. (f) The application of the H-sensor for gesture translation of sign language alphabet.**

length) and the temperature change of the conductive tendril during the power on (electric voltage of 0.55 V/cm for 12s, normalized to the contour length of the conductive tendril) and power off under load stress of 24 KPa (normalized to the cross-section area of the conductive tendril). Clearly, the electric power caused the temperature rise to an ultimate temperature of 187 °C due to Joule heating (infrared image characterization in Figure S18), and as expected in eq 2, also accompanied by proportional contraction ratio increase. Under the same load stress, the contraction stroke and ultimate temperature under varying electric voltage are displayed in Figure 4d. With the electric voltage increasing from 0.12 to 0.55 V/cm (corresponding to electric power from 0.026 to 0.525 W/cm, see Figure S19), the ultimate temperature increased from 28 to 187 °C, and the contraction stroke also increased from 2.5 to 19.8% (of loaded length) or from 4.6 to 37% (of nonloaded length). Next, under the specific electric voltage input (0.55 V/cm for 12s), the actuation performance was tested under different load



DOI: 10.1021/acsnano.8b01372
ACS Nano 2018, 12, 3898−3907

stress. As seen in Figure 4e, the load stress increased from 12 to 72 KPa, with the ultimate temperature located around 180 °C. The largest contraction stroke was obtained at a load stress of 24 KPa (photographs of actuation process in Figure S20), being as high as 19.8% (of loaded length) or 37% (of nonloaded length), comparable to the typical value of mammalian skeletal muscle (20%).[34] Besides, the contraction stroke of 10% (of loaded length) under load stress of 72 KPa meant that the conductive tendril could lift ~120 times its own weight by strain of 10% (photographs of actuation process in Figure S21). As contraction actuators, the conductive tendrils not only delivered consistent actuation performance under cyclic electric power input (see Figure S22) but also survived stretch test at strain of 1000% up to 100 cycles, with a minute contraction stroke degradation from 19.8 to 18.1%, as seen in Figure 4f. Also, the completely under water actuation of the conductive tendril was verified by working as a contractive underwater vibrator (frequency of 1 Hz, contraction stroke of 5%) under load stress of 36 KPa (see Movie S6), which greatly enriched the deployment environments of the conductive tendril as actuators.

The excellent actuation performance of the conductive tendrils empowered their further deployment as artificial muscles in practical applications. As proof-of-concept demonstrations, the conductive tendrils can not only work independently as an elastic dragger (Figure 5a) but also carry out programmable and sophisticated motility in an integrative level as a smart gripper (Figure 5c). Specifically, in Figure 5b, when triggered by a pulse electric input (0.9 V/cm for 0.8s), the elastic dragger pulled the load 60 times its own weight forward by 4.5 cm on ground (Movie S7). Even under water, the elastic dragger could still pull the same load forward by 3.2 cm (Figure S23 and Movie S8). In Figure 5d, three conductive tendrils were integrated into a smart gripper (photograph in Figure S24), with the lower two controlling the clasping and unclasping, the upper one controlling the lifting and dropping down. When electric power was applied on the lower and the upper conductive tendrils in succession, the gripper clasped and lifted the target object; when electric power on the upper and lower ones was turned off successively, the gripper put down and unclasped the target (see Movie S9). The conductive tendrils as artificial muscles hold great potential in designing diverse complicated motility by virtue of their outstanding features including low driving voltage (typically within 1 V/cm), large contraction stroke (19.8%), reliable adaptation to different application environments (on ground and under water), and the functional robustness against extreme deformations (stretch strain of 1000%).

**The Conductive Tendrils as Ultrastretchable Wearable Strain Sensors.** Encouraged by the combination of mechanical compliance, large stretch range, and stable conductance, we introduced another conductive PE yarn into the prestretched rubber layer during the fabrication of the conductive tendrils with prestrain of 0 and 100%, to obtain the straight and helical capacitive strain sensors, respectively (photographs of the sensors in Figure S25, detailed fabrication in Experimental Methods). The two conductive PE yarns serve as two stretchable electrodes and the polymer interlayer as the dielectric layer, similar to the design of parallel plate capacitive strain sensors. Figure 6a,b displays the schematic diagram of the helical sensor (H-sensor) structure and the SEM image of the cross section, respectively. The effective strain sensing ranges of the straight sensor (S-sensor) and the H-sensor are determined in Figure 6c, which gives the curves of the relative capacitance variation *versus* the tensile strain (see full response curves in Figure S26). Compared with the strain sensing range of 70% for the S-sensor, the H-sensor exhibits a tremendously expanded sensing range of 760%. To the best of our knowledge, this helical strain sensor outperforms all of the previously reported capacitive strain sensors in terms of the strain sensing range,[35−40] such as a printed AgNW-based film sensor (sensing range of 50%),[38] a buckled CNT-based fiber sensor (200%),[39] and a transparent CNT-based parallel plate sensor (300%).[36] This large strain sensing range of the H-sensor stems from the widely employed strategy of "structures that stretch", which enables considerably enhanced stretch range compared with another strategy of "materials that stretch", although accompanied by more complicated structure design and processing.[41,42] Reliable durability of sensing performance for both the S-sensor (testing strain of 60%) and the H-sensor (tensing strain of 600%) was confirmed in Figure 6d, which revealed no observable signal degradation after 1000 testing cycles. Besides, excellent sensing signal reproducibility across the whole sensing range was also proved for the S-sensor (Figure S27) and the H-sensor (Figure S28), accompanied by fast response times of ~50 and ~100 ms, respectively (Figure S29).

The conductive tendril-based strain sensors hold great prospect in wearable sensing applications, and two examples including sleep quality monitoring and gesture translation of the sign language alphabet are demonstrated. We attached the S-sensor onto the chest position of the volunteer, and the real-time capacitance response signals of breathing and turning over could be clearly captured and differentiated, as seen in Figure 6e and Movie S10. This can be exploited to assist the assessment of sleep quality and also to serve as an early warning sensor for sudden infant death syndrome and sleep apnea in adults.[43] We also integrated H-sensors into an electronic glove (E-glove, Figure S30), with each H-sensor fixed onto each E-glove finger. The finger bending induced strain change could be effectively transferred to the H-sensor. Through preliminary calibration, the response signal ranges for three finger-bending states including straight, half-bending, and full-bending could be acquired (Figure S31). When the letters "H", "E", "L", and "P" were expressed using the E-glove according to the sign language of alphabet (photographs in Figure 6f), the response signals of each finger were recorded (Table S1). Based on the calibration of finger bending states and the recorded signals, the hand gesture could be reconstructed as shown in the insets of Figure 6f (colors of gray, green and blue denoted bending states of straight, half-bending, and full bending, respectively), which accurately corresponded to the expressions of the specific letters. The E-glove possesses extensive potential in applications of human−machine interaction, smart robotics, and prosthetics.

## CONCLUSION

Through imitating the coiling mechanism, the conductive tendril borrowed the same configuration from the climbing plant tendril and successfully inherited the structure-related elastic buffering connection effect for its application in ultrastretchable electronics. The incorporation of the helical conductive PE yarn, as the dynamic element, also enabled the conductive tendril to work as artificial muscles in a fast, controllable, and reversible manner. In contrast, its counterpart in nature exhibits contraction motion in a one-time and relatively much slower way. Moreover, sensing ability was



DOI: 10.1021/acsnano.8b01372
ACS Nano 2018, 12, 3898−3907

developed by taking advantage of the combinational properties of the conductive tendril. These exceptional features and functions stemmed from the exquisite fusion of the artificial functional materials (conductive PE yarns) with the intelligent structure from nature (climbing plant tendril), and this can give us profound inspiration in the development of biomimetic materials science.

In summary, a conductive tendril is designed to mimic the functional merits of plant tendril. The conductivity and mechanical properties of the conductive tendrils can be tuned with ease. The tendril structure provides considerable leeway to extend the stretching range from strains of 225% to 2000%, accompanied by a small resistance increase of 9.2%, which made it competent in applications of ultrastretchable electronics, such as the ultrastretchable LED lighting and earphone audio cable. The conductive tendril also revealed excellent actuation performance: delivering contraction stroke of 19.8% or lifting 120 times its own weight. As artificial muscles, it could not only work independently as an elastic dragger but also realize programmable and complicated motility in an integrative manner, such as a smart gripper. Lastly, the modified conductive tendril possessed superb strain sensing capability with a large sensing range of 760% and was further exploited as wearable sensors for sleep quality monitoring and E-glove for gesture translation of the sign language alphabet. This work potentially paths the future cross-disciplinary inquest between plant biology and engineering to inspire and stimulate the design of new adaptive structures, soft robotics, and integrated electromechanical control systems.

## EXPERIMENTAL METHODS

**The Fabrication of the Conductive Tendril.** The schematic diagram of the fabrication process is shown in Figure S1. First, pristine helical PE yarns on the commercially available covered yarns were treated through hot alkali hydrolysis by soaking in NaOH (3.4% w/v, AR, Schedelco) at 130 °C for 2 h and then stripped off directly, to obtain treated PE yarn, which had a more compact and consolidated helical structure with a decreased diameter from 750 to 580 $\mu$m. Then the treated PE yarn was coated with different conductive materials including RGO, MWCNT, Ag particle, and AgNW *via* solution coating strategy. The resultant conductive PE yarn was further aligned on the surface of a prestretched silicone rubber film (Ecoflex 00-30) with thickness of 0.5 mm, then liquid precursor silicone rubber (Ecoflex 00-30) was coated on the upper surface of the prestretched substrate to infiltrate and encapsulate the conductive PE yarn. After cured in the oven (75 °C, 10 min), the upper (~0.6 mm in thickness) and the prestretched layers bonded together to form a straight strip, or the straight conductive tendril. When the prestretch was released, the straight strip self-coiled, with a handedness perversion in between oppositely handed helices with equal number. This coiled conductive tendril can be easily tuned to wholly left-handed or right-handed by inserting extra numbers of twist.

**The Solution Coating of Different Conductive Materials.** For RGO coating, the treated PE yarn was first dip-coated in graphene oxide[44] (GO) dispersion (1.4 mg/g in water) for specific times. GO coated on to the surface of PE yarn easily because of the hydrophilic nature. Then it was soaked (100 °C, 30s) in hydriodic acid (HI, 57 wt %, TCI Chemicals) to reduce GO to RGO. The RGO-based conductive PE yarn was rinsed with ethanol and then dried in an oven at 120 °C for 20 min to remove the residual HI acid. For MWCNT coating, treated PE yarn was dip-coated in MWCNT (XFM01, XFNANO) dispersion (2 mg/mL in water, sodium dodecyl sulfonate as dispersing agent at 10 mg/mL) for specific times and then dried in an oven at 100 °C for 1 h. For Ag particle coating, typically, 0.01 mol of $AgNO_3$ (AR, AnalaR NORMAPUR) was dissolved in 50 mL deionized water at room temperature to prepare a clear solution in beaker, and then 50 mL of 0.2 mol/L NaOH (AR, Schedelco) solution was added to the $AgNO_3$ solution, giving a brown precipitate. At this moment, the treated PE was immersed into the above solution. After that, ammonia solution (28%, Fisher Scientific) was added dropwise into the mixed solution under vigorous stirring until the brown precipitate just dissolved. 50 mL of 0.4 mol/L glucose (≥99.5%, Sigma) solution was then added to the mixture with vigorous stirring. The beaker was transferred to a water bath at 90 °C for 5 min. The Ag particle-based conductive PE yarn was obtained after washing with DI water, ethanol, and drying. For AgNW coating, the treated PE yarn was dip-coated in AgNW dispersion (1 wt % in ethanol, XFNANO) for specific times and then annealed in an oven at 120 °C for 30 min.

**The Fabrication of S-Sensor and H-Sensor.** The fabrication of the sensors was similar to that of the conductive tendril, except that one more conductive PE yarn was introduced into the prestretched rubber layer. First, conductive PE yarn (based on AgNW with normalized resistance of 0.5 Ω/cm to the length of the conductive PE yarn) was aligned straight on a glass slide, then liquid precursor silicone rubber (Ecoflex 00−30) was coated on the glass slide to infiltrate and encapsulate the porous conductive PE yarn. After curing (75 °C, 10 min), it was prestretched to a strain of 0% or 100%, then another silicone rubber layer with conductive PE yarn embedded was bonded on the upper surface of the prestretched one. After curing (75 °C, 10 min) and prestretch release, the S-sensor and H-sensor were obtained, respectively. The two conductive PE yarns served as the stretchable electrodes, with copper wire connected at the ends for external electrical connection.

**Characterization.** The SEM characterization was accomplished using a JEOL JSM-7001F field emission scanning electron microscope. The stress−strain curves of the conductive tendrils were tested with an electronic universal testing machine (CMT6103, MTS Systems (China) Co., Ltd.). The electric resistance was measured using an electrometer (Keithley 6517B). The stretching and bending tests were conducted using a high-precision motorized linear stage (LEYG, Electric Actuator, SMC). The twisting test was assisted by a homemade motorized rotation stage. For actuation test, a SourceMeter (Keithley 2602) was used to apply programmable electric power, and the actuation process was analyzed by frame-by-frame analysis method. The temperature was recorded using an IR camera (FLIR E50). For testing the strain sensing properties, the sensors were fixed onto a high-precision motorized linear stage (LEYG, Electric Actuator, SMC), and the capacitance response was measured using a LCR meter (TH2830).

## ASSOCIATED CONTENT

### Supporting Information

The Supporting Information is available free of charge on the ACS Publications website at DOI: 10.1021/acsnano.8b01372.

Movies S1−S5 (ZIP)
Movies S6−S10 (ZIP)
Figures S1−S31, the modeling and fitting of the tendril coiling, the measurement of the spring constant of the conductive tendrils, the mechanism analysis of the actuation of the conductive tendrils (PDF)

## AUTHOR INFORMATION

### Corresponding Author

*E-mail: elehgw@nus.edu.sg.

### ORCID

Jing Sun: 0000-0003-1101-1584
Ghim Wei Ho: 0000-0003-1276-0165

### Author Contributions

⊥These authors contributed equally.

### Notes

The authors declare no competing financial interest.



DOI: 10.1021/acsnano.8b01372
ACS Nano 2018, 12, 3898−3907

## ACKNOWLEDGMENTS

This research is supported by the NUS Hybrid-Integrated Flexible (Stretchable) Electronic Systems Program grant number R-263-501-011-731.

## REFERENCES

(1) Elbaum, R.; Zaltzman, L.; Burgert, I.; Fratzl, P. The Role of Wheat Awns in the Seed Dispersal Unit. *Science* **2007**, *316*, 884−886.
(2) Grassly, N. C.; Fraser, C.; Garnett, G. P. How the Venus flytrap Snaps. *Nature* **2005**, *433*, 417−421.
(3) Armon, S.; Efrati, E.; Kupferman, R.; Sharon, E. Geometry and Mechanics in the Opening of Chiral Seed Pods. *Science* **2011**, *333*, 1726−1730.
(4) Gerbode, S. J.; Puzey, J. R.; McCormick, A. G.; Mahadevan, L. How the Cucumber Tendril Coils and Overwinds. *Science* **2012**, *337*, 1087−1091.
(5) Meloche, C. G.; Knox, J. P.; Vaughn, K. C. A Cortical Band of Gelatinous Fibers Causes the Coiling of Redvine Tendrils: a Model Based upon Cytochemical and Immunocytochemical Studies. *Planta* **2007**, *225*, 485−498.
(6) Bowling, A. J.; Vaughn, K. C. Gelatinous Fibers Are Widespread in Coiling Tendrils and Twining Vines. *Am. J. Bot.* **2009**, *96*, 719−727.
(7) Chen, P.; Xu, Y.; He, S.; Sun, X.; Pan, S.; Deng, J.; Chen, D.; Peng, H. Hierarchically Arranged Helical Fibre Actuators Driven by Solvents and Vapours. *Nat. Nanotechnol.* **2015**, *10*, 1077−1083.
(8) Zhao, Y.; Miao, X.; Lin, J.; Li, X.; Bian, F.; Wang, J.; Zhang, X.; Yue, B. Coiled Plant Tendril Bioinspired Fabrication of Helical Porous Microfibers for Crude Oil Cleanup. *Global Challenges* **2017**, *1*, 1600021.
(9) Erb, R. M.; Sander, J. S.; Grisch, R.; Studart, A. R. Self-Shaping Composites with Programmable Bioinspired Microstructures. *Nat. Commun.* **2013**, *4*, 1712.
(10) De Haan, L. T.; Verjans, J. M.; Broer, D. J.; Bastiaansen, C. W.; Schenning, A. P. Humidity-Responsive Liquid Crystalline Polymer Actuators with an Asymmetry in the Molecular Trigger That Bend, Fold, and Curl. *J. Am. Chem. Soc.* **2014**, *136*, 10585−10588.
(11) Jiang, S.; Liu, F.; Lerch, A.; Ionov, L.; Agarwal, S. Unusual and Superfast Temperature-Triggered Actuators. *Adv. Mater.* **2015**, *27*, 4865−4870.
(12) Na, J. H.; Evans, A. A.; Bae, J.; Chiappelli, M. C.; Santangelo, C. D.; Lang, R. J.; Hull, T. C.; Hayward, R. C. Programming Reversibly Self-Folding Origami with Micropatterned Photo-Crosslinkable Polymer Trilayers. *Adv. Mater.* **2015**, *27*, 79−85.
(13) Wang, M.; Lin, B. P.; Yang, H. A Plant Tendril Mimic Soft Actuator with Phototunable Bending and Chiral Twisting Motion Modes. *Nat. Commun.* **2016**, *7*, 13981.
(14) Iamsaard, S.; Asshoff, S. J.; Matt, B.; Kudernac, T.; Cornelissen, J. J.; Fletcher, S. P.; Katsonis, N. Conversion of Light into Macroscopic Helical Motion. *Nat. Chem.* **2014**, *6*, 229−235.
(15) Yang, R.; Zhao, Y. Non-Uniform Optical Inscription of Actuation Domains in a Liquid Crystal Polymer of Uniaxial Orientation: An Approach to Complex and Programmable Shape Changes. *Angew. Chem., Int. Ed.* **2017**, *56*, 14202−14206.
(16) Guo, H.; Cheng, J.; Wang, J.; Huang, P.; Liu, Y.; Jia, Z.; Chen, X.; Sui, K.; Li, T.; Nie, Z. Reprogrammable Ultra-Fast Shape-Transformation of Macroporous Composite Hydrogel Sheets. *J. Mater. Chem. B* **2017**, *5*, 2883−2887.
(17) Kim, D.; Lee, H. S.; Yoon, J. Highly Bendable Bilayer-Type Photo-Actuators Comprising of Reduced Graphene Oxide Dispersed in Hydrogels. *Sci. Rep.* **2016**, *6*, 20921.
(18) McMillen; Goriely. Tendril Perversion in Intrinsically Curved Rods. *J. Nonlinear Sci.* **2002**, *12*, 241−281.
(19) Isnard, S.; Silk, W. K. Moving with Climbing Plants from Charles Darwin's Time into the 21st Century. *Am. J. Bot.* **2009**, *96*, 1205−1221.
(20) Macdougal, D. T. The Mechanism of Curvature of Tendrils. *Ann. Bot.* **1896**, *10*, 373−402.
(21) Smyth, D. R. Helical Growth in Plant Organs: Mechanisms and Significance. *Development* **2016**, *143*, 3272−3282.
(22) Pieranski, P.; Baranska, J.; Skjeltorp, A. Tendril Perversion-a Physical Implication of the Topological Conservation Law. *Eur. J. Phys.* **2004**, *25*, 613−621.
(23) Ibrahim, N. A.; Eid, B. M.; Youssef, M. A.; Ameen, H. A.; Salah, A. M. Surface Modification and Smart Functionalization of Polyester-Containing Fabrics. *J. Ind. Text.* **2013**, *42*, 353−375.
(24) Timoshenko, S. Analysis of Bi-Metal Thermostats. *J. Opt. Soc. Am.* **1925**, *11*, 233−255.
(25) Yamada, T.; Hayamizu, Y.; Yamamoto, Y.; Yomogida, Y.; Izadi-Najafabadi, A.; Futaba, D. N.; Hata, K. A Stretchable Carbon Nanotube Strain Sensor for Human-Motion Detection. *Nat. Nanotechnol.* **2011**, *6*, 296−301.
(26) Zang, J.; Ryu, S.; Pugno, N.; Wang, Q.; Tu, Q.; Buehler, M. J.; Zhao, X. Multifunctionality and Control of the Crumpling and Unfolding of Large-Area Graphene. *Nat. Mater.* **2013**, *12*, 321−325.
(27) Shin, U.-H.; Jeong, D.-W.; Park, S.-M.; Kim, S.-H.; Lee, H. W.; Kim, J.-M. Highly Stretchable Conductors and Piezocapacitive Strain Gauges Based on Simple Contact-Transfer Patterning of Carbon Nanotube Forests. *Carbon* **2014**, *80*, 396−404.
(28) Won, Y.; Kim, A.; Yang, W.; Jeong, S.; Moon, J. A Highly Stretchable, Helical Copper Nanowire Conductor Exhibiting a Stretchability of 700%. *NPG Asia Mater.* **2014**, *6*, e132.
(29) Zhang, Z.; Deng, J.; Li, X.; Yang, Z.; He, S.; Chen, X.; Guan, G.; Ren, J.; Peng, H. Superelastic Supercapacitors with High Performances During Stretching. *Adv. Mater.* **2015**, *27*, 356−362.
(30) Guan, L.; Nilghaz, A.; Su, B.; Jiang, L.; Cheng, W.; Shen, W. Stretchable-Fiber-Confined Wetting Conductive Liquids as Wearable Human Health Monitors. *Adv. Funct. Mater.* **2016**, *26*, 4511−4517.
(31) Jang, N.-S.; Kim, K.-H.; Ha, S.-H.; Jung, S.-H.; Lee, H. M.; Kim, J.-M. Simple Approach to High-Performance Stretchable Heaters Based on Kirigami Patterning of Conductive Paper for Wearable Thermotherapy Applications. *ACS Appl. Mater. Interfaces* **2017**, *9*, 19612−19621.
(32) Liu, Z. F.; Fang, S.; Moura, F. A.; Ding, J. N.; Jiang, N.; Di, J.; Zhang, M.; Lepro, X.; Galvao, D. S.; Haines, C. S.; Yuan, N. Y.; Yin, S. G.; Lee, D. W.; Wang, R.; Wang, H. Y.; Lv, W.; Dong, C.; Zhang, R. C.; Chen, M. J.; Yin, Q.; et al. Hierarchically Buckled Sheath-Core Fibers for Superelastic Electronics, Eensors, and Muscles. *Science* **2015**, *349*, 400−404.
(33) Choy, C. L.; Chen, F. C.; Young, K. Negative Thermal Expansion in Oriented Crystalline Polymers. *J. Polym. Sci., Polym. Phys. Ed.* **1981**, *19*, 335−352.
(34) Mirfakhrai, T.; Madden, J. D. W.; Baughman, R. H. Polymer Artificial Muscles. Mater. *Mater. Today* **2007**, *10*, 30−38.
(35) Cohen, D. J.; Mitra, D.; Peterson, K.; Maharbiz, M. M. A Highly Elastic, Capacitive Strain Gauge Based on Percolating Nanotube Networks. *Nano Lett.* **2012**, *12*, 1821−1825.
(36) Cai, L.; Song, L.; Luan, P.; Zhang, Q.; Zhang, N.; Gao, Q.; Zhao, D.; Zhang, X.; Tu, M.; Yang, F.; Zhou, W.; Fan, Q.; Luo, J.; Zhou, W.; Ajayan, P. M.; Xie, S. Super-Stretchable, Transparent Carbon Nanotube-Based Capacitive Strain Sensors for Human Motion Detection. *Sci. Rep.* **2013**, *3*, 3048.
(37) Stoyanov, H.; Kollosche, M.; Risse, S.; Wache, R.; Kofod, G. Soft Conductive Elastomer Materials for Stretchable Electronics and Voltage Controlled Artificial Muscles. *Adv. Mater.* **2013**, *25*, 578−583.
(38) Yao, S.; Zhu, Y. Wearable Multifunctional Sensors Using Printed Stretchable Conductors Made of Silver Nanowires. *Nanoscale* **2014**, *6*, 2345−2352.
(39) Choi, C.; Lee, J. M.; Kim, S. H.; Kim, S. J.; Di, J.; Baughman, R. H. Twistable and Stretchable Sandwich Structured Fiber for Wearable Sensors and Supercapacitors. *Nano Lett.* **2016**, *16*, 7677−7684.
(40) Atalay, A.; Sanchez, V.; Atalay, O.; Vogt, D. M.; Haufe, F.; Wood, R. J.; Walsh, C. J. Batch Fabrication of Customizable Silicone-Textile Composite Capacitive Strain Sensors for Human Motion Tracking. *Adv. Mater. Technol.* **2017**, *2*, 1700136.
(41) Jason, N. N.; Ho, M. D.; Cheng, W. Resistive Electronic Skin. *J. Mater. Chem. C* **2017**, *5*, 5845−5866.



DOI: 10.1021/acsnano.8b01372
*ACS Nano* 2018, 12, 3898−3907

(42) Gong, S.; Cheng, W. One-Dimensional Nanomaterials for Soft Electronics. *Adv. Electron. Mater.* **2017**, *3*, 1600314.
(43) Schechtman, V. L.; Harper, R. M.; Kluge, K. A.; Wilson, A. J.; Hoffman, H. J.; Southall, D. P. Cardiac and Respiratory Patterns in Normal Infants and Victims of the Sudden Infant Death Syndrome. *Sleep* **1988**, *11*, 413−496.
(44) Hummers, W. S.; Offeman, R. E. Preparation of Graphitic Oxide. *J. Am. Chem. Soc.* **1958**, *80*, 1339−1339.



DOI: 10.1021/acsnano.8b01372
*ACS Nano* 2018, 12, 3898−3907